Applications in Energy and Combustion Science 27 (2026) 100526

Contents lists available at ScienceDirect

Applications in Energy and Combustion Science

journal homepage: www.elsevier.com/locate/jaecs

Non-premixed ammonia combustion in porous media to promote thermal cracking of NH_3: A low-emission burner concept

D. Kretzler [a,*], R. Puri [a], B. Stelzner [a], T. Zirwes [b], G. Vignat [c], F.P. Hagen [a], O.T. Stein [a], M. Ihme [c,d,e], D. Trimis [a]

[a] Karlsruhe Institute of Technology, Engler-Bunte-Institute, Combustion Technology, Karlsruhe, D-76131, Germany
[b] University of Stuttgart, Institute for Reactive Flows, Stuttgart, D-70569, Germany
[c] Stanford University, Department of Mechanical Engineering, Stanford, CA 94305, USA
[d] SLAC National Accelerator Laboratory, Department of Photon Science, Menlo Park, CA 94025, USA
[e] Stanford University, Department of Energy Science and Engineering, Stanford, CA 94305, USA

ARTICLE INFO

Keywords:
Ammonia combustion
Non-premixed combustion
Porous media burner
NO_x emissions

ABSTRACT

This study investigates spatially-distributed, non-premixed ammonia/air combustion in porous media burners (PMBs) as a strategy to mitigate NO_x emissions and improve flame stability, two key challenges for ammonia as a carbon-free fuel. To the best of our knowledge, this is the first experimental demonstration of this approach. Experiments are conducted over global equivalence ratios ($0.7 \leq \Phi_g \leq 1.3$) and thermal loads ($0.25 \leq P \leq 0.76\ \mathrm{MW\,m^{-2}}$). Temperatures inside the porous matrix and global emissions of NO_x, NH_3, N_2O, and H_2 are measured and compared between non-premixed and premixed operation. Results show that NH_3/air flames are stably anchored in high-porosity foams (15 PPI) without external preheating. N_2O emissions remain below 40 ppmv (normalized to 15 % O_2), and non-premixed operation reduces NO_x by one order of magnitude compared to premixed operation, while maintaining low NH_3 slip. Low NH_3 and NO_x emissions occur only in non-premixed operation, with the most favorable regimes under globally fuel-lean conditions. In the lowest non-premixed case (31 ppmv NH_3, 111 ppmv NO_x, $P = 0.25\ \mathrm{MW\,m^{-2}}$, $\Phi_g = 0.8$), NO_x is reduced by 90 % compared to premixed operation (2 ppmv NH_3, 1148 ppmv NO_x) at identical conditions. Complementary volume-averaged simulations (VAS) reproduce these trends and indicate that H_2 formed in NH_3-rich zones promotes NO_x reduction. These findings demonstrate that spatially-distributed, non-premixed combustion in PMBs enables stable, low-emission ammonia combustion and may further reduce NH_3 slip through improved downstream mixing and residence time control.

1. Introduction

Ammonia has attracted growing attention as a carbon-free energy carrier, offering promising potential for energy storage, transportation, and conversion [1,2]. For direct energy conversion, NH_3 can alternatively be cracked into H_2 prior to use. However, this route introduces an additional endothermic conversion stage and associated balance-of-plant losses, which typically reduces the overall efficiency compared to direct NH_3 combustion [3]. This highlights the need for a burner design that enables the combustion of pure NH_3/air mixtures which is addressed by a porous inert media burner (PMB) concept in the present work. Several drawbacks hinder the widespread burner application of ammonia: low chemical reactivity, resulting in low flame speed and difficult stabilization, and elevated levels of unburned NH_3 and nitrogen-based pollutants. Specifically, NO_x formation tends to dominate under fuel-lean conditions, while fuel-rich operation typically leads to excessive NH_3 slip [2,4–6]. Moreover, in contrast to the combustion of conventional fuels under atmospheric pressure, NH_3 combustion also leads to the formation of N_2O. Although nitrous oxide appears in lower concentrations than NO_x, its strong greenhouse effect, with a 20-year global warming potential more than 200 times greater than that of CO_2, necessitates its inclusion in emission assessments [4,7,8]. Consequently, future regulations may also impose strict limits on N_2O emissions [9,10]. Additionally N_2O has a high ozone layer depletion potential [11]. These considerations highlight the need for advanced combustion concepts that enable stable and low-emission ammonia conversion.

Recent stabilization strategies have often focused on swirl burners [2,6,12] or hydrogen enrichment [1,5] but both routes struggle with

* Correspondence to: Engler-Bunte-Ring 7, Karlsruhe, 76131, Germany.
E-mail address: daniel.kretzler@kit.edu (D. Kretzler).

https://doi.org/10.1016/j.jaecs.2026.100526
Received 22 February 2026; Received in revised form 10 June 2026; Accepted 11 June 2026
Available online 16 June 2026

the fundamental trade-off between NO_x emissions and NH_3 slip [13]. Moreover, in premixed flames, hydrogen addition often leads to increased NO_x and N_2O formation [5,7]. As a result, fuel staging strategies have come into focus, which suppress pollutants by leveraging fuel-rich zones to limit NO_x formation and fuel-lean zones to reduce NH_3 emissions [2,4,14].

Another promising concept is premixed combustion in porous inert media. In such systems, thermal recirculation between the combustion zone and the incoming flow is substantially increased by the heat transport properties of the porous body, leading to a higher effective flame propagation speed. This enhancement arises from heat recirculation mechanisms involving conduction, convection, and radiation within the solid matrix [15–17]. Specifically, the effective flame speed can rise by an order of magnitude, depending on the material properties and boundary conditions [18–20]. Hence, porous burners are highly suitable for the flame stabilization of low-calorific gases. [18,21]. Stable premixed combustion of pure ammonia/air mixtures in porous media has already been demonstrated. However, high pollutant emissions were observed in such PMB systems, especially under practically relevant lean operating conditions: Wang et al. [22] reported NO_x emissions exceeding 5000 ppmv (6 % O_2), and Vignat et al. [23,24] reported more than 1500 ppmv NO_x (15 % O_2). An exception was reported by Vignat et al. [14], who achieved emissions as low as 28 ppmv NO_x and 149 ppmv NH_3 (15 % O_2) in a downstream, two-stage operation concept. In general, pollutant emissions in porous inert media burners (PMBs) can be optimized by adjusting thermal properties and the flow field [17,25,26]. Reducing NH_3 slip, in particular, demands high temperatures, lean equivalence ratios, and uniform reactant mixing [24,27]. Nevertheless, fuel-bound NO_x formation remains a key challenge, especially because the conventional Zel'dovich mechanism plays only a minor role in NH_3/air combustion [2,4].

Recent investigations have explored non-premixed ammonia combustion as a possible route to reduce NO_x emissions. Kretzler et al. [28] investigated non-premixed NH_3/air flames in a heated slot burner with high-temperature walls, achieving NO_x emissions as low as 335 ppmv (normalized to 15% O_2) under globally stoichiometric conditions. Zhang et al. [29] examined a non-premixed swirl-stabilized flame with 30 Vol % hydrogen addition, achieving NO_x concentrations below 30 ppmv and unburned NH_3 levels below 1500 ppmv (normalized to 15% O_2). Similarly, Chen et al. [30] reported sub-100 ppmv NO_x and NH_3 emissions using a laminar non-premixed preheated flame (above 640 K). These results highlight the potential of non-premixed strategies for pollutant reduction. Further addressing these challenges requires advanced burner designs to ensure stable and low-pollutant combustion for NH_3 use in large-scale applications. Although existing studies demonstrate the suitability of PMBs for stabilizing pure NH_3/air flames, PMBs without secondary staging exhibit NO_x emissions of several thousand ppmv under lean or stoichiometric operating conditions.

To address these challenges, the objective of the present work is to deliver a first proof-of-concept demonstration of spatially-distributed, non-premixed NH_3/air combustion in a PMB to enhance flame stabilization by heat recirculation and reduce NO_x emissions by thermal NH_3 decomposition under fuel rich conditions avoiding the fuel-bound NO_x formation pathways. Focus is set on (i) mapping flame-stability limits through variation of thermal load and equivalence ratio, (ii) quantifying temperatures within the porous media (iii) measuring global emissions of NO_x, NH_3, N_2O and formed H_2, and (iv) numerically predicting exhaust gas composition and analyzing the associated global NO formation pathways. Performance is compared to a reference case with premixed combustion in the same porous medium to assess whether the non-premixed PMB concept can pair flame stability with low NO_x, as well as overall low-pollutant output.

The remainder of this paper is organized as follows. First, the conceptual approach is introduced in Section 2.1, followed by the burner designs in Section 2.2 and the determination of their effective material properties in Section 2.3. The experimental setup and diagnostics are described in Section 2.4 followed by the introduction of the numerical model in Section 2.5, including the governing equations of the volume-averaged approach and the simulation setup. Results on flame stabilization, pollutant emissions, and analysis of pollutant formation are discussed in Section 3.1, Section 3.2, and Section 3.3, respectively, followed by conclusions in Section 4.

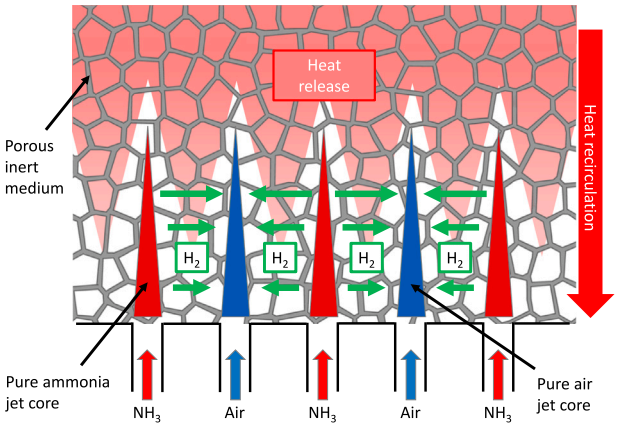

Fig. 1. Conceptual illustration of spatially-distributed, non-premixed NH_3/air combustion in porous inert media. Spatially separated NH_3 (red) and air (blue) jets are heated by radiative-conductive heat recirculation, promoting thermal cracking to H_2, which diffuses toward oxidizer-rich regions and burns locally.

2. Methods

2.1. Conceptual approach

Ammonia flames stabilized in porous inert media show enhanced stability [24], and non-premixed operation might be a promising approach to reduce NO_x formation [28–30]. To combine these advantages, the present study implements spatially-distributed, non-premixed combustion in a PMB. Fig. 1 presents an overview of the proposed concept. Distributed, spatially separated jets of NH_3 and air penetrate the porous medium, and the initial absence of mixing prevents immediate oxidation. Intense radiative-conductive heat recirculation from the solid is expected to raise the core jet temperature above ≈ 1000 K, where thermal cracking of ammonia becomes relevant, leading to its partial decomposition into hydrogen and nitrogen [31,32]: $2\,NH_3 \rightleftharpoons N_2 + 3H_2$. The produced hydrogen, characterized by a markedly higher diffusivity than ammonia, diffuses toward the oxidizer stream, where combustion occurs. A fraction of the released heat is recirculated to sustain further NH_3 dehydrogenation and hydrogen production in locally rich regions, creating a self-sustained reaction zone. Because the dominant heat release originates from the oxidation of H_2 formed via NH_3 dehydrogenation, and because O_2 is consumed before reaching NH_3-rich regions, the formation of fuel-bound NO_x is inherently suppressed. In this study, a PMB is investigated in spatially-distributed, non-premixed operation, and its combustion characteristics are compared with those under premixed conditions.

2.2. Porous inert media burners

Experiments are conducted in a cylindrical PMB (see Fig. 2) that contains a stack of four SiSiC foams (EngiCer SA) with pore densities of 15, 10, 10, and 20 pores per inch (PPI), each 50 mm in diameter and 25 mm thick. The porosity of the foams is approximately 80 % (exact properties of the porous foams obtained from μ-X-ray computed tomography (XCT) scans are provided in Table 2). The foams are arranged within a quartz tube and are wrapped with 6 mm ceramic-fiber

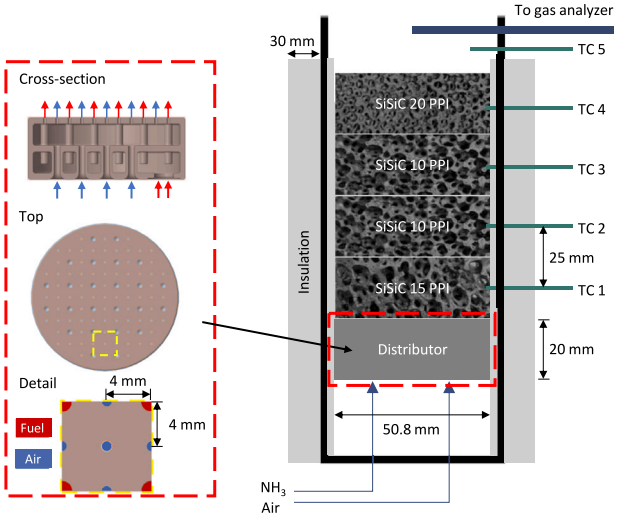

Fig. 2. Schematic of the experimental apparatus showing the gas distributor, including its arrangement and cross-sectional view, for non-premixed operation. SiSiC: silicon-infiltrated silicon carbide; PPI: Pores Per Inch; TC: thermocouple.

paper (ACE 1500, Kager) to minimize heat loss. A 30 mm vacuum-formed ceramic shell (KFB1400, Becker Insulation) further insulates the quartz tube. The primary objective of the burner design is to facilitate stable, low-emission non-premixed NH_3 combustion by fostering thermal cracking in locally fuel-rich regions and ensuring rapid mixing and complete burnout downstream. Specifically, insulation of this relatively small-size burner reduces heat losses, leading to higher combustion temperatures and enhanced reactant preheating, thereby improving flame stabilization during pure NH_3 combustion. In addition, the porous matrix is tailored such that the upstream foam induces relatively low dispersion to maintain the integrity of the fuel jets and promote NH_3 cracking in locally fuel-rich regions. Downstream sections with larger pore size and thicker struts promote higher dispersion and improved mixing. The final section, featuring a stepwise-graded pore size (10 to 20 PPI), enhances heat recirculation and minimizes heat loss to the surroundings [33]. Heat loss remains the predominant factor contributing to incomplete NH_3 combustion in porous media under premixed conditions [27]. Therefore, minimizing these losses is essential for the complete conversion of ammonia.

Two different gas distribution configurations are used for premixed and non-premixed operation, respectively. For the non-premixed configuration, a stainless-steel gas distributor with a height of 20 mm and a diameter of 50.8 mm, fabricated via metal laser melting (1.4404, 50 µm layer thickness, 3D-Laserdruck GmbH & Co. KG) is employed. This design is optimized for homogeneous flow distribution. The fuel ducts contain 24 holes, each with a diameter of 1.4 mm, while the air ducts include 77 holes with a diameter of 1 mm (see Fig. 2). The pressure drop across these holes is large compared to the pressure variations inside the plenums, which ensures an approximately uniform flow distribution. During manufacturing, imperfections at the outlet holes caused by 3D printing are removed by manual reworking. In addition, the leak tightness between the fuel and air supply is checked using an exhaust gas probe directly at the outlet holes, and no defects are detected. For premixed operation, a second, identical burner configuration is used, in which the gas distributor is replaced by a perforated ceramic-fiber plate (HT 180, Duotherm) with identical external dimensions and 1 mm holes arranged in the same pattern. This plate serves as a flame arrester, thereby ensuring consistency in flow distribution for comparison between non-premixed and premixed operation and preventing flashback. In the premixed configuration, the gas supply is provided through a single pipe feeding an externally premixed NH_3/air mixture into the comparatively large hollow plenum (80 mm in height) between the perforated plate and the glass flange at the bottom. This plenum also contains a flow straightener consisting of two laser-cut stainless steel meshes (mesh sizes 0.3 and 0.2 mm; wire diameters 0.2 and 0.125 mm; Dorstener Drahtwerke), ensuring homogeneous mixture formation and a uniform flow distribution.

Table 1
Operating parameters of µ-XCT scans.

Parameter (unit)	Value
X-ray voltage (kV)	150
X-ray current (µA)	70
Voxel size (µm)	39
Scan size (voxels)	1600 × 1380 × 624

Table 2
Geometric and thermal properties of the porous foams employed in this study.

Pore density (PPI)	10	15	20	Dist.
Thickness L (mm)	25	25	25	20
Porosity ε[a] (%)	76.9	72.9	75.1	4.4
Pore diameter d_p[a] (mm)	3.34	2.85	2.38	–
Specific surface S_v[a] (m^{-1})	714	891	1075	261
Tortuosity η[a] (–)	1.31	1.48	1.45	1
Axial effective thermal conductivity factor a[a] ($Wm^{-1}K^{-1}$)	0.094	0.074	0.073	0.968
Extinction coefficient κ[b] (m^{-1})	525	650	831	400

Dist.: Distributor
[a] Values for the porous zones obtained from µ-XCT scans
[b] Values obtained from ray-casting radiation simulations.

2.3. Determination of effective material properties

The effective properties and closure models defined in the governing equations in Section 2.5.1 depend on the material and macro-structure of the porous medium. Effective properties of the porous zones are extracted from µ-X-ray computed tomography (XCT) scans acquired with a CT-ALPHA X-ray scanner (ProCon X-ray) equipped with a Dexela Type 1512 detector (Perkin Elmer). Scan parameters are summarized in Table 1. Micro-X-ray computed tomography is an X-ray imaging technique with (sub)micron resolution based on a cone-beam X-ray source and a rotating sample holder [34]. The acquired 2D projections are reconstructed into a 3D voxel dataset with gray values proportional to X-ray attenuation. Post-processing with the open-source software PuMA [35] is used to determine porosity, pore diameter, and specific surface area. Background noise in the scans is suppressed with a 3D Gaussian filter, and segmentation threshold values between gas and solid phases are determined using the Otsu method [36]. The dispersion length cannot be measured directly. Its role in the calculation of the energy balance and pollutant formation is discussed in [37]. For this work, the characteristic dispersion length is taken as $d_{\mathrm{disp}} = 0.1 d_p$, where d_p is the characteristic pore diameter. The axial effective thermal-conductivity coefficient a, as well as the tortuosity η, are determined with PuMA's finite volume solver. Extinction coefficients κ are obtained from ray-casting radiation simulations. Additionally, the perforated plate in the premixed configuration is also modeled as a porous medium. Table 2 compiles the properties for each porous zone and the distributor.

The heat transfer coefficient h_v for all zones is calculated as

$$h_v = Nu \frac{S_v \lambda}{d_h}\,, \tag{1}$$

where the Nusselt numbers Nu for SiSiC porous zone (pz) and distributor (dist.) [38] are defined as

$$Nu_{\mathrm{pz}} = 3.7 Re^{0.38} Pr^{0.25} ,$$
$$Nu_{\mathrm{dist.}} = 3.66 + \frac{0.065(PrRe(d_h/L))^{1.117}}{1 + 0.031(PrRe(d_h/L))^{0.779} Pr^{0.25}} , \quad (2)$$

and the Reynolds Re and Prandtl Pr numbers are

$$Re = \frac{\rho|\vec{u}|d_h}{\mu} , \quad Pr = \frac{c_p \mu}{\lambda} . \quad (3)$$

For porous zones, the hydraulic diameter is $d_h = 4\gamma/S_v$, and for the distributor, it is taken as the diameter of the holes. The effective thermal conductivity λ_{eff} [39–41] is calculated as

$$\lambda_{\mathrm{eff,pz}} = a\lambda_{s,\mathrm{ref}} \left(\frac{T_s}{T_0}\right)^b , \quad \lambda_{\mathrm{eff,dist.}} = a(c_1 + c_2 T_s) , \quad (4)$$

where $\lambda_{s,\mathrm{ref}} = 110\ \mathrm{Wm^{-1}K^{-1}}$ is the thermal conductivity of SiSiC at $T_0 = 293$ K, the factor a is given in Table 2 and $b = -0.53$. For the perforated ceramic-fiber plate (HT 180, Duotherm), the coefficients are $c_1 = 2.72 \times 10^{-2}\ \mathrm{Wm^{-1}K^{-1}}$ and $c_2 = 10^{-4}\ \mathrm{Wm^{-1}K^{-2}}$. The permeability coefficients k_1 and k_2 are calculated from [42,43] for the porous zones and the distributor, respectively.

2.4. Experimental setup and diagnostics

The gas flow rates are controlled using mass flow controllers (MFCs, Bronkhorst) with a relative accuracy better than 0.5%. The MFCs are factory-calibrated and serviced in regular intervals. The stated uncertainty corresponds to the manufacturer's specification. For the fuel stream, pure NH_3 (Air Liquide) with a purity better than 99.98% is supplied. To ensure continuous gas flow, the liquefied NH_3 cylinders remain at room temperature using a heating system.

To measure the exhaust gas species, a sampling probe with heated transfer lines is positioned centrally at the burner outlet. Gas analyzers (ABB, response time < 4 s) are used to detect N_2O (0–500 ppmv, Uras 26), O_2 (0–25 Vol %, Uras 26) and H_2 (0–10 Vol %, Caldos 17) in the dry gas phase. NH_3 (0–2000 ppmv), NO (0–5000 ppmv), and NO_2 (0–1000 ppmv) are measured in the wet gas phase using a heated Limas 21 analyzer to avoid losses due to dissolution of NO_x and NH_3 in water condensate. If the measuring range of a species is exceeded, the exhaust gas is diluted with heated air to enable detection. To ensure comparability, all species are normalized to 15 % O_2 following [44]:

$$X_{i,15\%\mathrm{O_2}} = X_i \frac{X_{\mathrm{O_2,air}} - X_{\mathrm{O_2}}^{\mathrm{ref}}}{X_{\mathrm{O_2,air}} - X_{\mathrm{O_2}}^{\mathrm{meas}}} , \quad (5)$$

with $X_{\mathrm{O_2,air}} = 20.95\%$ and $X_{\mathrm{O_2}}^{\mathrm{ref}} = 15.0\%$. For species reported on a wet-gas basis, the corresponding dry-basis O_2 measurements are first converted to a wet-gas basis before normalization to 15 % O_2. Since direct H_2O measurement is not available in the present setup, the H_2O mole fraction required for the wet-to-dry conversion is estimated from a simplified stoichiometric exhaust gas balance. For the base evaluation, the oxidized NH_3 fraction is assumed to form N_2 and H_2O, while under fuel-rich conditions ($\Phi_g > 1$) the non-oxidized NH_3 fraction is assumed to decompose completely to N_2 and H_2, i.e., NH_3 slip is neglected. To ensure comparability with values reported on a dry-gas basis, the wet-gas emission values reported in this study can be converted using the corresponding conversion factor $f_{\mathrm{wet\to dry}}$, summarized in Table 3. The uncertainty associated with possible NH_3 slip under fuel-rich conditions was assessed by a bounding analysis using two limiting cases, namely complete NH_3 slip and the assumed complete decomposition of the unburned NH_3 to N_2 and H_2. For all operating points considered in this work ($\Phi_g = 0.7 - 1.3$), the resulting difference in the wet-to-dry conversion factor remained below 2.3 %, with the maximum deviation occurring at $\Phi_g = 1.3$. This conservative upper bound is also consistent with the corresponding numerical predictions presented in this study, which suggest that deviations in the exhaust gas H_2O fraction remain small across the investigated operating range.

Signal acquisition relies on a NI-9208 current-input module housed in a NI-DAQ-9179 chassis. All data are averaged over at least 2 min after reaching steady state conditions. Due to the low standard deviations of the averaged data, the measurement uncertainties are estimated solely based on the manufacturer's specifications, yielding $\Delta X_{\mathrm{NH_3}} = 20$ ppmv, $\Delta X_{\mathrm{NO}} = 50$ ppmv, $\Delta X_{\mathrm{NO_2}} = 10$ ppmv, $\Delta X_{\mathrm{N_2O}} = 5$ ppmv, $\Delta X_{\mathrm{H_2}} = 0.2$ Vol % and $\Delta X_{\mathrm{O_2}} = 0.125$ Vol %. Zero calibration prior to each measurement was performed using high-purity nitrogen (99.999 %, Air Liquide). Span calibration was performed using certified calibration gases for N_2O (500 ppmv) and H_2 (10 Vol %, Air Liquide, relative measurement uncertainty 2 %), ambient air (20.95 Vol % O_2) for O_2, and internal calibration cells for NH_3, NO, and NO_2 in the heated Limas 21 analyzer, corresponding to 80 % of the respective measurement ranges. This procedure was applied prior to each measurement series to account for analyzer drift. Additionally, the uncertainty arising from the normalization to 15 % O_2, as defined in Eq. (5), is consistently taken into account. The resulting compound error in the normalized concentration $X_{i,15\%\mathrm{O_2}}$, arising from ΔX_i and $\Delta X_{\mathrm{O_2}}^{\mathrm{meas}}$ is calculated using the Gaussian error propagation:

$$\Delta X_{i,15\%\mathrm{O_2}} = \sqrt{\left(\frac{\partial X_{i,15\%\mathrm{O_2}}}{\partial X_i}\Delta X_i\right)^2 + \left(\frac{\partial X_{i,15\%\mathrm{O_2}}}{\partial X_{\mathrm{O_2}}^{\mathrm{meas}}}\Delta X_{\mathrm{O_2}}^{\mathrm{meas}}\right)^2} , \quad (6)$$

which, applied to Eq. (5), yields:

$$\Delta X_{i,15\%\mathrm{O_2}} = \left[\left(\frac{20.95 - 15.0}{20.95 - X_{\mathrm{O_2}}^{\mathrm{meas}}}\Delta X_i\right)^2 + \left(\frac{20.95 - 15.0}{(20.95 - X_{\mathrm{O_2}}^{\mathrm{meas}})^2} X_i \Delta X_{\mathrm{O_2}}^{\mathrm{meas}}\right)^2\right]^{1/2} . \quad (7)$$

Uniform exhaust gas distribution across the outlet cross section was confirmed, with measured variations in NH_3 and NO_x emissions below 5 % based on sampling at various radial outlet positions.

Temperature measurements were conducted using five S-type thermocouples (PtRh-Pt; IEC 60584 class 1, 0.3 mm thermo wire) inserted into a ceramic protection tube (d = 1.55 mm, Degussit AL23, Kyocera Fineceramics Europe GmbH) and connected to a NI-9214 thermocouple module. The data acquisition system was operated in accordance with the manufacturer's recommended calibration interval. Four of the thermocouples were positioned within the axial centers of the ceramic foams, 25 mm apart and inserted 5 mm into the porous matrix, while the fifth thermocouple measures the temperature at the burner outlet. To suppress catalytic effects of the platinum, the thermocouple tips are coated with zirconium oxide (Resbond 904, Cotronics). Temperature measurements over time are used together with species measurements to evaluate burner stability and to assess whether stationary conditions are reached. At each operating point, the burner is operated until no systematic temporal variations are observable in the measured temperatures and emissions, for at least 10 min. Additionally, to ensure comparability with operating points reported for similar burner designs in terms of shape and dimensions (Vignat et al. [23,24]), an operating point is only considered stationary and thus stable if the temperature fluctuations on all thermocouples installed in the burner remain below

Table 3
Conversion factors obtained from the stoichiometric combustion of NH_3 for converting wet-gas values to dry-gas values.

Φ_g (–)	$X_{\mathrm{H_2O}}$ (Vol %)	$f_{\mathrm{wet\to dry}}$ (–)
0.7	23.61	1.309
0.8	26.25	1.356
0.9	28.74	1.403
1.0	31.11	1.452
1.1	29.87	1.426
1.2	28.72	1.403
1.3	27.67	1.382

10 K over two minutes. Before each measurement, the burner is pre-heated to its operating temperature with a methane/air flame. It is then switched to NH_3/air operation and allowed to stabilize until stationary conditions are achieved. Further, temperature data also locate the flame position.

2.5. Volume-averaged numerical model

2.5.1. Governing equations

A volume-averaged approach [37,39] is utilized to simulate reactive flow in porous media. The volume-averaged governing equations are written as

$$\frac{\partial(\gamma\rho)}{\partial t} + \nabla\cdot(\gamma\rho\vec{u}) = 0\ , \tag{8}$$

$$\frac{\partial(\gamma\rho\vec{u})}{\partial t} + \nabla\cdot(\gamma\rho\vec{u}\vec{u}) = -\gamma\nabla p + \nabla\cdot(\gamma\boldsymbol{\tau}) - \vec{u}_{\text{sup}}\left(\frac{\mu}{k_1} + \frac{\rho}{k_2}|\vec{u}_{\text{sup}}|\right)\ , \tag{9}$$

where $\vec{u}$ is the interstitial gas velocity, ρ the density, p the pressure, γ the porosity, $\vec{u}_{\text{sup}} = \gamma\vec{u}$ the superficial velocity and $\boldsymbol{\tau}$ the stress tensor. The last term on the RHS of Eq. (9) is the Darcy–Forchheimer term for pressure loss due to flow through the porous material. k_1 and k_2 are the linear and turbulent permeability coefficients, respectively. To consider the effect of heat transfer to and from the solid structure, the energy equation for the gas phase can be written in terms of total enthalpy as

$$\frac{\partial(\gamma\rho h_{\text{tot}})}{\partial t} + \nabla\cdot(\gamma\rho\vec{u}h_{\text{tot}}) = \nabla\cdot(\gamma\vec{q}) + \gamma\frac{\partial p}{\partial t} - \gamma\sum_k(h_k^0\dot{\omega}_k) - h_v(T - T_s)\ , \tag{10}$$

where h_v is the heat transfer coefficient and the total energy is $h_{\text{tot}} = h_{\text{sens}} + \frac{1}{2}\vec{u}\cdot\vec{u}$, with the sensible enthalpy h_{sens}. Eq. (10) accounts for flow dispersion by the solid matrix and the heat flux reads

$$\vec{q} = \underbrace{-(D_{\text{disp}}\rho)\nabla h_{\text{sens}}}_{\text{dispersion}} + \underbrace{\sum_k h_{\text{sens},k}\hat{\vec{j}}_k}_{\text{differential diffusion}} \underbrace{-\frac{\lambda}{\eta}\nabla T}_{\text{Fourier}}\ , \tag{11}$$

where λ is the thermal conductivity of the gas, c_p the isobaric heat capacity, η the tortuosity, k the index of the kth species, $h_{\text{sens},k}$ the sensible enthalpy of species k and $\hat{\vec{j}}_k = \vec{j}_k - Y_k\sum_k\vec{j}_k$ the conservative molecular diffusive species flux. The dispersion coefficient is calculated as

$$D_{\text{disp}} = \frac{1}{2}|\vec{u}|d_{\text{disp}}\ , \tag{12}$$

where d_{disp} is the characteristic dispersion length. The gas species conservation equation reads

$$\frac{\partial(\gamma\rho Y_k)}{\partial t} + \nabla\cdot(\gamma\rho(\vec{u} + \vec{u}_c)Y_k) = \gamma\dot{\omega}_k - \nabla\cdot(\gamma\vec{j}_k)\ , \tag{13}$$

where Y_k is the mass fraction and $\dot{\omega}_k$ is the reaction rate of species k, $\vec{j}_k$ the diffusive flux. The correction velocity is given by $\vec{u}_c = -\frac{1}{\rho}\sum_k\vec{j}_k$. The diffusive fluxes are expressed as:

$$\vec{j}_k = -\rho\left(\frac{D_{m,k}^{\text{mole}}}{\eta} + D_{\text{disp}}\right)\nabla Y_k - Y_k\rho\frac{D_{m,k}^{\text{mole}}}{\bar{M}\eta}\nabla\bar{M}\ , \tag{14}$$

where $\bar{M}$ is the mean molar mass of the mixture, and the diffusion coefficient is

$$D_{m,k}^{\text{mole}} = \frac{1 - Y_k}{\sum_{j\neq k}\frac{X_j}{D_{j,k}}}\ , \tag{15}$$

where X_j is the mole fraction and $D_{j,k}$ the binary diffusion coefficient. The energy equation for the solid phase reads

$$(1-\gamma)\rho_s c_s\beta\frac{\partial T_s}{\partial t} = \nabla\cdot(\lambda_{s,\text{eff}}\nabla T_s) + \nabla\cdot(\lambda_{\text{rad}}\nabla T_s) + h_v(T - T_s) - \zeta(T_s - T_{\text{ref}})\ , \tag{16}$$

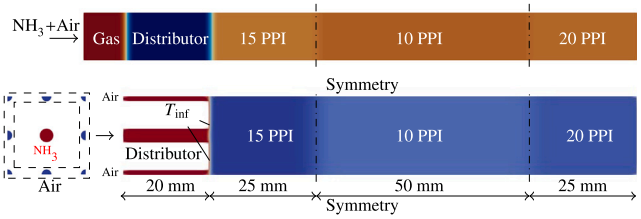

Fig. 3. Burner schematic for VAS of NH_3/air combustion in porous media. Premixed (top, 1D) and non-premixed (bottom, 2D cut through 3D domain) operating condition.

Table 4
Inlet and interface boundary conditions for $P = 0.51$ MW m^{-2}. The subscripts "PRM" and "NPR" refer to premixed and non-premixed, respectively.

Φ_g (–)	$\dot{m}_{in,PRM}$ (kgm^{-2}s^{-1})	$Re_{\text{in,PRM}}$ (–)	$\dot{m}_{\text{in,air,NPR}}$ (kgm^{-2}s^{-1})	$Re_{\text{in,air,NPR}}$ (–)	T_{inf} (K)
0.8	0.225	14.8	6.68	1790	1322
0.9	0.203	13.5	5.94	1590	1325
1.0	0.185	12.4	5.34	1430	1327
1.1	0.171	11.5	4.86	1300	1290
1.2	0.159	10.7	4.45	1191	1263

where c_s is the heat capacity of the solid, $\lambda_{s,\text{eff}}$ the effective thermal conductivity of the solid. The thermal conductivity λ_{rad} for the radiative heat transfer is defined using the Rosseland model [45] as $\lambda_{\text{rad}} = 16\sigma T_s^3/(3\kappa)$, with σ the Stefan–Boltzmann constant and κ the extinction coefficient. The numerical coefficient $0 \leq \beta < 1$ accelerates convergence to the steady state. The heat loss of the porous burner is modeled using heat loss coefficient ζ and $T_{\text{ref}} = 300$ K.

2.5.2. Simulation setup

The burner configurations used for volume-averaged simulations (VAS) are shown in Fig. 3. One-dimensional simulations (1D-VAS) are performed for premixed cases, whereas the non-premixed cases are simulated in three dimensions to accurately represent the spatial distribution of ammonia and air inlet holes from the experiment. The distributor is resolved as channels with a fixed interface temperature T_{inf}. The term "interface" here refers to the interface between the distributor and the most upstream (15 PPI) SiSiC layer. Both premixed and non-premixed cases are simulated for a thermal load of $P = 0.51$ MW m^{-2} with an inlet temperature of $T_{\text{in}} = 300$ K and radiative heat loss at the outlet. Symmetry boundary conditions are used for the patches normal to the burner axis.

The inlet mass flux and the interface temperatures are defined based on the experimental measurements. The fixed boundary conditions for the inlets and distributor are given in Table 4. The total inlet fuel mass flux $\dot{m}_{\text{in,f,np}} = 1.45$ kg m^{-2}s^{-1} ($Re_{\text{in,f,np}} = 566$) is fixed for all operating points. Heat loss coefficients ζ for each porous zone are adjusted in the numerical model to approach the thermo-couple measurements in the experiments. The 1D computational domain is discretized into 1,300 cells. For 3D-VAS, the computational domain is locally refined in the channels and the reaction zone, discretizing into a total of 112,525 cells. A total of five detailed chemical-kinetic mechanisms for ammonia/air combustion, namely Stagni [46], NUIG [47], KAUST [48], Konnov [49,50] and Shrestha [51] are used and compared.

3. Results

3.1. Flame stabilization

As already discussed in Section 1, combustion in porous media enhances flame stability and is particularly suitable for the stabilization of low-calorific gases [15–17], favoring pure NH_3/air combustion without

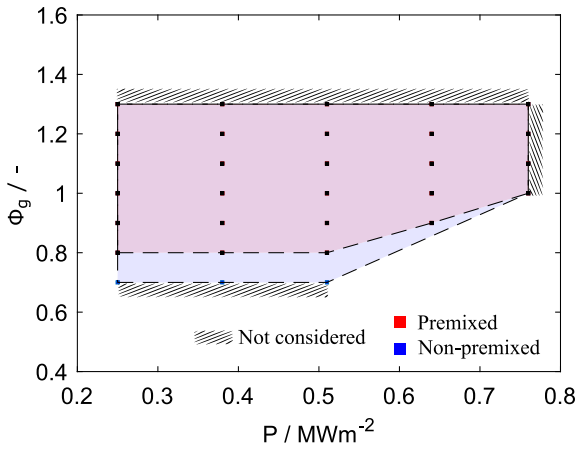

Fig. 4. Experimental stability map for pure NH_3/air combustion in the porous burners, shown as a function of the global equivalence ratio Φ_g and thermal load per unit surface P (based on the fuel lower heating value). Symbols mark operating points where stable combustion is achieved. The blue region indicates conditions where the non-premixed operation is stable, whereas the red region is entirely contained within it and corresponds to the premixed operation. No flame could be stabilized outside the considered regions.

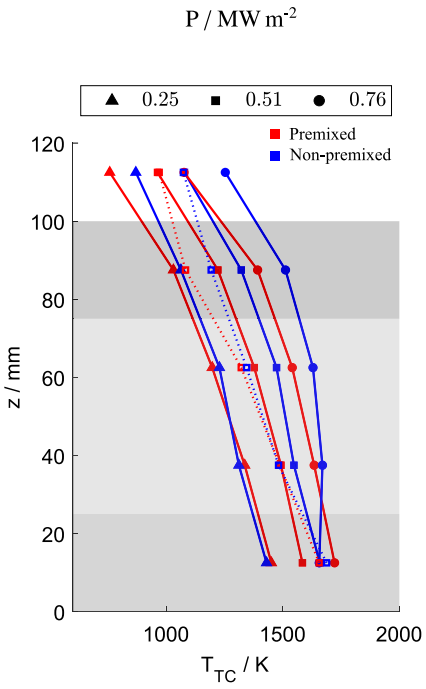

Fig. 5. Temperature profiles T_{TC} along the height of the burner z under global stoichiometric conditions $\Phi_g = 1$ for non-premixed and premixed operation at varying thermal loads P of 0.25, 0.51 and 0.76 MW m^{-2} (see legend), based on thermocouple measurements (solid lines). Predicted temperatures using the NUIG mechanism (dotted lines) are shown for $P = 0.51$ MW m^{-2}.

H_2 enrichment or external preheating. This section evaluates overall burner stability and the differences in stability between non-premixed and premixed operation modes as a function of the global equivalence ratio Φ_g, evaluated from the total NH_3 and air flow rates supplied to the burner, and the thermal load per unit surface P.

Both operating modes are investigated using the stability criteria defined in Section 2.4. The investigated operating domain is limited to $0.7 \leq \Phi_g \leq 1.3$ and $P \leq 0.76$ MW m^{-2} due to safety and material constraints. Step sizes of $\Delta\Phi_g = 0.1$ and $\Delta P = 0.1275$ MW m^{-2} define the test matrix. The resulting stability map is presented in Fig. 4. The present burner enables pure NH_3/air combustion in porous media with pore densities as high as 10/15 PPI. This is likely due to the enhanced thermal insulation of the burner, which supports NH_3 flame stabilization more effectively than in the configurations reported by Vignat et al. [14,23,24], who achieved stable combustion for pore densities of 3 PPI with comparable burner designs in terms of shape and dimensions. Fig. 4 demonstrates stable combustion up to $P = 0.76$ MW m^{-2}. Operating points outside the considered stable region result in flame extinction or blow-off. Based on this operating window, the turndown ratio, defined as the ratio of the highest and lowest mass flux sustaining combustion, is ≈ 1:4. Note that the matrix is limited to $\Phi_{g,max} = 1.3$ and $P_{max} = 0.76$ MW m^{-2}, so the potential of this NH_3 porous burner is not fully exploited yet. Industrial burners typically target high turndown ratios, and premixed CH_4 PMBs commonly achieve ratios of 1:10–1:15 [24]. Thermal power density per surface area is an important parameter for minimizing device size, weight and cost. While premixed CH_4 porous burners at atmospheric pressure reach up to 4.0 MW m^{-2}, with typical values not exceeding 3.0 MW m^{-2} [18], the present laboratory-scale pure NH_3/air burner was tested up to 0.76 MW m^{-2} in the considered operating matrix. Referencing the full reactor length yields a volumetric power density of 7.6 MW m^{-3}, and limiting the reference length to the 40 mm heat-release zone – conservatively defined as the region where most heat is released – raises this value to 19 MW m^{-3}, comparable to the 5–22 MW m^{-3} reported for swirled NH_3/H_2 flames [24].

Relative to the premixed operation, the non-premixed operation shows a wider lean stability limit. At $P < 0.51$ MW m^{-2}, stable operation extends down to $\Phi_g = 0.8$ (premixed) and $\Phi_g = 0.7$ (non-premixed). Both windows narrow as P increases, converging at $\Phi_g = 1.0$ and $P = 0.76$ MW m^{-2}. While the lean stability limit for premixed operation is comparable to that observed by Vignat et al. [24], the non-premixed operation at $\Phi_g = 0.7$ exhibits a wider lean stability limit for pure NH_3/air flames. The extended lean stability limit in the non-premixed operation most likely results from mixture stratification, which induces locally stoichiometric conditions and thus higher temperatures, thereby stabilizing the reaction zone. Upstream dehydrogenation of NH_3 to H_2 (see Section 3.3, Fig. 9) may further enhance stability, as the formed H_2 broadens the narrow NH_3/air flammability range ($\Phi = 0.63–1.4$) toward the much wider range of H_2/air ($\Phi = 0.1–7.1$) [4]. The convergence of the stability limits at $P = 0.76$ MW m^{-2} likely results from the onset of flame lift-off as well as from the step size of the test matrix.

The location of the flame can be approximated based on the temperature profiles within the porous medium. Fig. 5 shows that the measured porous body temperatures increase with thermal power for both operating modes, as the heat release rate increases more than the accompanying heat losses. The highest measured temperature, observed at $\Phi_g = 1$ and $P = 0.76$ MW m^{-2} under premixed operation, is 1722 K and thus noticeably below the corresponding adiabatic value of 2071 K [4], indicating the presence of heat losses. Note that gas temperature is not measured directly, and the thermocouple tip temperature is assumed to approximate the solid matrix temperature rather than the gas temperature [21]. At low and medium thermal powers ($P < 0.51$ MW m^{-2}), both operating modes exhibit similar temperature profiles, and the flame front is located in the lowest foam layer (15 PPI), as indicated by the temperature maximum. For $P \geq 0.51$ MW m^{-2}, the non-premixed operation shows higher downstream temperatures, suggesting that the flame stabilizes progressively farther downstream. Numerical predictions of the temperature profiles at the medium power setting are in good agreement with the measurements and reproduce the observed flame stabilization in the lowest foam layer.

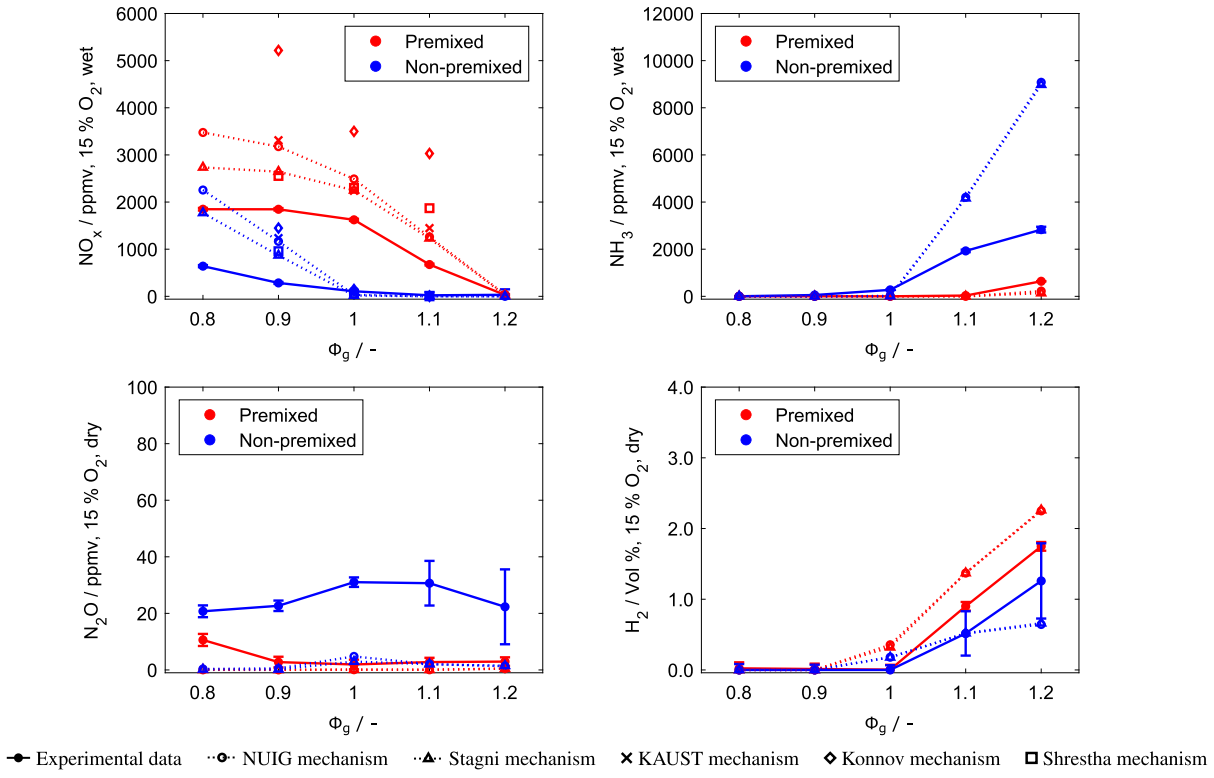

Fig. 6. Measured exhaust gas emissions at the burner outlet at 0.51 MW m^{-2} normalized to 15 % O_2 following [44], shown as a function of the global equivalence ratio Φ_g for the premixed and non-premixed operation, comparing experimental data with VAS predictions using the NUIG and Stagni kinetic mechanisms. Additional NO_x predictions using the KAUST [48], Konnov [49,50] and Shrestha [51] mechanisms for selected equivalence ratios Φ_g = 0.9, 1.0 and 1.1 are also reported.

3.2. Pollutant emissions

In this section, we focus on global emissions at the stable operating points, following the procedure described in Section 2.4. Fig. 6 presents the measured and predicted NO_x, NH_3, N_2O, and H_2 emissions from the PMB, normalized to 15 % O_2, as a function of the equivalence ratio at the intermediate thermal load of $P = 0.51$ MW m^{-2}.

For NO_x, emissions rise at $\Phi_g \leq 1$ and decrease under rich conditions, reflecting the transition from the "pollutant pathway" in lean NH_3 flames to the "N_2H_2 pathway" in rich flames [24,52]. Further, Vignat et al. [24] reported that, in porous burners, the balance between NO formation rate in the flame zone and its consumption in the post-flame region becomes more favorable as the mixture turns rich, leading to a reduction in global NO_x emissions. Across all operating points, non-premixed operation emits substantially – often an order of magnitude – less NO_x than premixed operation, supporting the hypothesis of the non-premixed PMB concept, i.e. upstream NH_3 dehydrogenation in rich regions followed by recombination to N_2 and H_2 suppressing fuel-bound NO_x (see Section 2.1). In addition, hydrogen produced in very rich regions can diffuse outwards and activate NH De-NO_x pathways. Furthermore, the non-premixed configuration yields a longer flame with reduced peak temperatures, further limiting thermal NO_x formation. However, thermal NO_x is not significant compared to fuel-bound NO_x. Additionally, hydrogen produced in very rich regions diffuses outwards, activating NH De-NO_x pathways. As expected, unburned NH_3 remains low for $\Phi_g < 1$ but strongly increases under fuel-rich conditions. Under non-premixed operation, NH_3 slip is higher than in the premixed case, most likely due to incomplete mixing in the downstream foam sections. An optimized flow geometry of the porous body, increasing dispersion and micro-mixing, or an extended reactor length providing increased residence time could lead to a complete burnout. Despite the current trade-off between significantly lower NO_x and slightly higher NH_3 emissions for the present non-optimized geometry, non-premixed operation offers a more favorable compromise. For instance, at stoichiometric conditions ($\Phi_g = 1$), the NO_x and NH_3 concentrations are approximately 107 ppmv and 275 ppmv, respectively, in non-premixed operation, compared to 1623 ppmv and 2 ppmv in premixed operation. In this case, the reduction in NO_x emissions is significantly larger than the increase in NH_3 slip. Non-zero H_2 concentrations appear for $\Phi_g > 1$ in both operating modes and are typically about an order of magnitude higher than the corresponding NH_3 slip. Because no external H_2 is added, this observation confirms substantial NH_3 dehydrogenation. This effect is most evident in the premixed case at $\Phi_g = 1.1$, where 0.9 % H_2 and only 36 ppmv unburned NH_3 are detected. For N_2O, no systematic dependence on Φ_g is observed in the non-premixed operation, whereas the premixed case shows a slight increase under lean conditions. Absolute levels remain higher under non-premixed operation, reaching up to 35 ppmv, compared with 11 ppmv in the premixed case. Nevertheless, for both operating modes N_2O emissions are insignificant both in terms of toxicity and greenhouse gas potential.

Overall, numerical predictions obtained with the five kinetic mechanisms are in qualitative and partially also quantitative agreement with the experimental results. For both premixed and non-premixed operation, the trends in NO_x and NH_3 emissions as well as H_2 concentrations at the outlet are reproduced, whereas deviations remain in the predicted N_2O emissions, particularly with respect to their peak levels. Differences are also observed between the numerical predictions: NO_x emissions predicted with the Stagni, NUIG, KAUST and Shrestha mechanisms are fairly similar, especially for $\phi = 1.0$. The NUIG and KAUST mechanisms predict higher NO emissions for lean conditions as compared to the Stagni and Shrestha mechanisms. The Konnov mechanism predicts significantly higher NO emissions, in particular for premixed burner operation. The addition of the chemiluminescence species and the enhanced flux of atomic nitrogen along the $NO_2 \rightarrow NO$

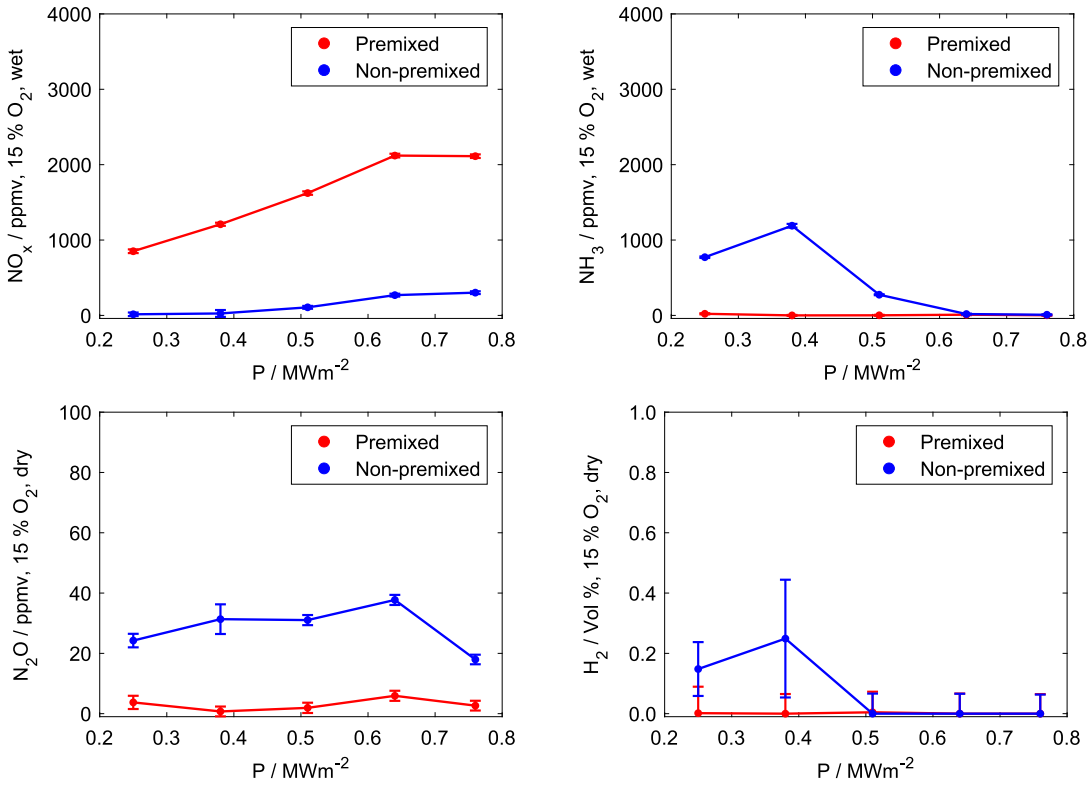

Fig. 7. Measured exhaust gas emissions at the burner outlet at $\Phi_g = 1$ normalized to 15 % O_2 following [44], shown as a function of the thermal load for premixed and non-premixed operation.

pathway (already observed in our previous work [28], see Fig. S1 therein) lead to overall higher NO production rates in the Konnov mechanism for the present conditions. The VAS predictions for the other species are very similar for all evaluated mechanisms (not shown for KAUST, Konnov and Shrestha in Fig. 6 for clarity of presentation).

Besides the previously investigated variation in equivalence ratio, changes in thermal load affect the temperature, heat recirculation, and flame surface power density within the burner. Its influence on pollutant emissions is examined in Fig. 7 for global stoichiometric operation ($\Phi_g = 1$). This condition is chosen because the flame remains stable across the entire power range while both NO_x and NH_3 are present. With increasing thermal load, the measured temperature rises from 1430 K to 1722 K in the 15 PPI foam ($z = 12.5$ mm). A similar trend is observed for NO_x emissions, which increase in both operating modes, consistent with previous findings [5,24].

Across all power levels, NO_x emissions remain substantially lower in non-premixed operation (down to 15 ppmv) than in premixed operation (down to 852 ppmv). NH_3 emissions remain close to the limit of detection (LOD) for premixed operation under stoichiometric conditions. In contrast, elevated NH_3 slip is observed under non-premixed operation, particularly at thermal loads below 0.64 MW m^{-2}, reaching up to 1190 ppmv. As the thermal load rises, unburned NH_3 concentrations fall to nearly zero, showing that – beyond the previously discussed benefits of longer residence time and better mixing – higher temperatures can also lead to complete NH_3 reforming. H_2 emissions are observed only in the presence of elevated NH_3 slip under non-premixed operation at low thermal loads. Note that possible non-uniformities at the non-premixed gas distributor could also lead to streaks of local fuel-rich zones over several fuel/air feed holes, causing elevated NH_3 emissions.

N_2O emissions show no systematic dependence on thermal load. However, the non-premixed operation reaches up to 40 ppmv, whereas the premixed operation remains below 10 ppmv across the tested range.

As previously noted, a trade-off between NO_x and NH_3 emissions exists across lean and rich conditions. To further investigate this trade-off and compare the overall emission behavior of the two operating modes, global NH_3 and NO_x emissions are plotted in Fig. 8 for all tested stable equivalence ratios and thermal loads. To achieve low-pollutant operation, an operating window in which the concentrations of both species are minimized must be targeted. Overall, N_2O remains at moderate levels of up to ≈ 40 ppmv and premixed operation yields significantly higher NO_x emissions, whereas non-premixed operation exhibits higher NH_3 slip. This slip can likely be reduced by improved mixing and longer residence times, as well as higher temperatures at lower relative heat losses through burner scale-up.

Nevertheless, the non-premixed map contains considerably more operating points that fall into a low-emission regime for both species compared to the premixed case. Emissions below 250 ppmv NH_3 or NO_x are only observed in non-premixed operation, with low-emission operation occurring predominantly under fuel-lean conditions, whereas the premixed case reaches its lowest concentrations under fuel-rich conditions. Lowest emissions occur in the lean region at $P = 0.25$ MW m^{-2} in non-premixed operation, where:

- 9 ppmv NH_3 and 285 ppmv NO_x at $\Phi_g = 0.7$,
- 31 ppmv NH_3 and 111 ppmv NO_x at $\Phi_g = 0.8$,
- 250 ppmv NH_3 and 42 ppmv NO_x at $\Phi_g = 0.9$.

Note that outside this subset, individual species concentrations can be even lower.

3.3. Analysis of pollutant formation

The conceptual approach introduced in Section 2.1 is validated from 3D-VAS of non-premixed ammonia/air combustion. The hydrogen and NO formation is further investigated for the operating point $\Phi_g = 0.9$ and $P = 0.51$ MW m^{-2}. This point with a medium thermal load and a global lean condition is chosen due to the significant reduction in NO_x emissions and negligible NH_3 slip, as observed in Fig. 6. Due to the heat re-circulation within the porous matrix, H_2 is produced from

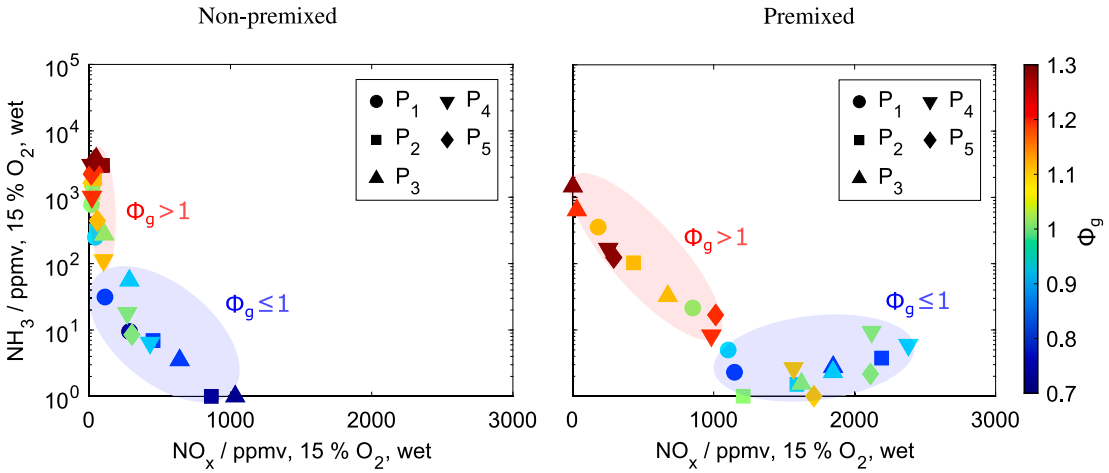

Fig. 8. Measured exhaust gas emissions at the burner outlet, normalized to 15 % O_2 following [44], shown as a function of the measured NO_x and NH_3 for varying equivalence ratio and thermal load ($P_1 - P_5$ = 0.25, 0.38, 0.51, 0.64 and 0.78 MW m^{-2}) in non-premixed (left) and premixed (right) operation. The blue region qualitatively marks the range where lean and stoichiometric mixtures ($\Phi_g \leq 1$) dominate, while the red region marks the range where rich mixtures ($\Phi_g > 1$) dominate, with a few outliers present in both regions.

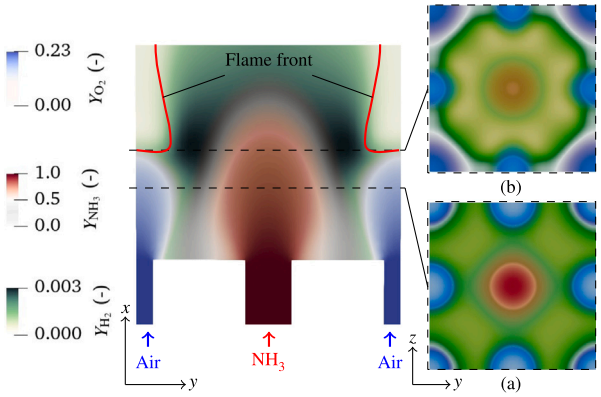

Fig. 9. Left: VAS prediction of ammonia dehydrogenation in non-premixed combustion at Φ_g = 0.9 and P = 0.51 MW m^{-2}. Right: Sectional plot normal to burner axis showing NH_3, H_2, and O_2 mass fractions for volume-averaged peak H_2 (a) production and (b) consumption rates.

ammonia upstream of the main reaction zone as illustrated in Fig. 9. The distribution of H_2 between the NH_3 and air jets is similar to the conceptual illustration in Fig. 1. Given the high temperature at the interface (1325 K for Φ_g = 0.9), dehydrogenation of NH_3 starts in the zone between the fuel and air channel outlets. In axial direction from the interface, the extent of the hydrogen production zone is 3 mm and the flame stabilizes itself at 3.3 mm. The ammonia conversion ratio in the zone upstream of the flame front is calculated as $\mathcal{F} = 2X_{H_2}/(2X_{H_2} + 3X_{NH_3})$ and defines the fraction of hydrogen converted from NH_3 to H_2. The flame front is defined by the maximum heat release rate. Upstream of the flame front, within the first few millimeters above the outlet, the volume-averaged simulation predicts an ammonia conversion ratio of up to $\mathcal{F}$ = 0.35.

The peak H_2 mass fraction Y_{H_2} = 0.003 in the sectional plane shown in Fig. 9 (a) is much lower compared to ammonia Y_{NH_3} = 0.93, but it contributes 40% to the net combustion process ($H_2 + OH \rightleftharpoons H + H_2O$). For the premixed operation, this contribution is 33%. For both operating modes, the major reactions leading to H_2 production were evaluated as:

$$H + NH_3 \rightleftharpoons H_2 + NH_2$$
$$H + NH_2 \rightleftharpoons H_2 + NH$$
$$H + NH \rightleftharpoons H_2 + N$$
$$H + N_2H_2 \rightleftharpoons H_2 + NNH$$
$$H + HNO \rightleftharpoons H_2 + NO$$

Volume-averaged hydrogen production rates in the production zone are 0.248 and 0.183 kg m^{-3}s^{-1} for non-premixed and premixed operation, respectively. Hydrogen produced from NH_3 is fully consumed in both operating modes as $H_2 + OH \rightleftharpoons H + H_2O$.

As was observed in Fig. 6, non-premixed ammonia/air combustion in porous media emits significantly lower NO compared to the premixed operation. The chemistry of NO formation is analyzed by performing a reaction pathway analysis (RPA) for the operating point Φ_g = 0.9 and P = 0.51 MW m^{-2}. Since all the evaluated reaction mechanisms (except Konnov) predict fairly similar NO emissions, see Fig. 6, the RPA for both non-premixed and premixed operation is solely performed using the Stagni and the NUIG mechanisms, with the corresponding path diagrams for NUIG shown in Fig. 10. The atomic N flux from NH_3 to N_2 follows three different pathways, shown with different colors in Fig. 10 [24]. The pollutant and the N_2H_2 path contribute to the bulk of the N flux to N_2 for both operation modes. However, the N_2H_2 path has a higher net share for the non-premixed (54%) operation compared to the premixed (46%) operation. In the Stagni mechanism, this share changes to 42% and 44% for non-premixed and premixed operation respectively. As shown in [24], under rich premixed conditions, the importance of this path for De-NO_x increases. Here, although the non-premixed burner is operated under globally lean conditions, the locally rich regions producing hydrogen activate this pathway, leading to overall lower NO_x emissions. However, the N_2H_2 path is less pronounced for the non-premixed operation in the Stagni mechanism, where the $N_2O \rightarrow N_2$ path contributes equal N flux to N_2. Negligible N_2O emission is calculated for both mechanisms as shown in Fig. 6. The major path for pollutant formation is HNO ⟶ NO, where the normalized N flux in premixed operation is twice that of non-premixed. The important reactions leading to the production of NO are H + HNO $\rightleftharpoons$ H_2 + NO, HNO $\rightleftharpoons$ H + NO, and HNO + NH_2 $\rightleftharpoons$ NH_3 + NO. The classical NO_x (Zel'dovich) pathway has a minimal contribution to the NO production for both operations. However, relatively higher peak gas temperatures in the premixed operation could also accelerate NO production. The share of the Zel'dovich pathway is more active and the share of the major HNO ⟶ NO path reduces in the Stagni mechanism for premixed operation. However, a higher share (15%) is calculated for the non-premixed operation as compared to the NUIG mechanism. The reactions NH+NO $\rightleftharpoons$ H+N_2O, N+NO $\rightleftharpoons$ N_2+O, and NH+NO $\rightleftharpoons$

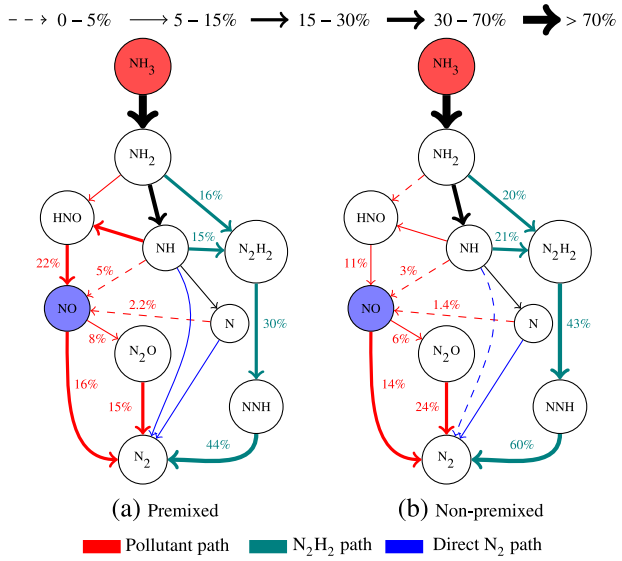

Fig. 10. Global space and time integrated NO pathways for $\Phi_g = 0.9$, $P = 0.51\ \mathrm{MW\,m^{-2}}$ visualized through N fluxes calculated using the NUIG mechanism in VAS. The thickness of the arrows indicates the normalized N flux (see legend above).

$N_2 + OH$ are responsible for the consumption of NO in both reaction mechanisms, where the reaction $NH + NO \rightleftharpoons H + N_2O$ is more active in the Stagni mechanism. The net production rate of NO for the non-premixed operation is $0.017\ \mathrm{kg\,m^{-3}s^{-1}}$ as compared to $0.047\ \mathrm{kg\,m^{-3}s^{-1}}$ for premixed combustion. The net NO production rates predicted by the Stagni mechanism are ≈ 30% lower for both operations. These net NO production rates explain the emissions reported in Fig. 6. Higher ammonia dehydrogenation improves the combustion characteristics for lean non-premixed ammonia/air operation and assists in reducing emissions. We note that ammonia combustion chemistry remains a significant source of uncertainty for quantitative NO_x predictions, so the results presented here should be interpreted in the context of the underlying kinetic mechanism.

4. Conclusions

This study presents a systematic investigation of spatially-distributed, non-premixed combustion of ammonia in porous inert media. A broad matrix of stable operating points for pure NH_3/air combustion was identified, and the corresponding temperatures within the porous media, as well as the global emissions of NO_x, NH_3, N_2O, and H_2 were quantified. The main findings are:

- This study presents, to the best of our knowledge, the first demonstration of spatially-distributed, non-premixed NH_3/air combustion in porous inert media, enhancing flame stabilization via thermal NH_3 cracking and reducing NO_x emissions by avoiding fuel-bound NO_x formation pathways.
- Stable NH_3/air flames are sustained without external preheating or fuel enrichment across a wide operating window, $0.7 \leq \Phi_g \leq 1.3$ and $0.25 \leq P \leq 0.76\ \mathrm{MW\,m^{-2}}$, with an extended lean stability limit in non-premixed operation down to $\Phi_g = 0.7$, compared to $\Phi_g = 0.8$ in premixed operation. This operating window could be further expanded by reducing relative heat losses.
- Relative to premixed operation, NO_x emissions are significantly reduced by approximately one order of magnitude, whereas unburned NH_3 in the present non-optimized setup increases slightly and N_2O remains at moderate levels of up to ≈ 40 ppmv.
- In contrast to premixed operation, the lowest emissions in non-premixed operation occur predominantly under globally fuel-lean conditions, making this strategy particularly attractive for industrial applications with compact, non-staged operation.
- Numerical predictions of exhaust gas composition at the medium power setting are in good qualitative and partially quantitative agreement with the experimental results and capture the observed trends. However, deviations in the predicted NO_x levels between the utilized reaction mechanisms are observed, with all mechanisms underpredicting the measured N_2O emissions.
- Global reaction pathway analysis conducted on the VAS data shows that under nominally lean operating conditions, the N_2H_2 De-NO_x path is more active in the non-premixed compared to the premixed case. This is typical for rich premixed operation, showing that the hydrogen produced in rich zones of the non-premixed burner adds to overall De-NO_x.

Overall, this study demonstrates spatially-distributed, non-premixed combustion in porous inert media as a promising concept for low pollutant operation and provides valuable information for optimizing flame stability and emission control in future ammonia-fueled systems. Further reductions in NH_3 slip should be attainable through improved mixing in the downstream foam sections, increased residence times, and temperature control.

CRediT authorship contribution statement

D. Kretzler: Writing – original draft, Methodology, Investigation, Formal analysis. **R. Puri:** Writing – review & editing, Software, Methodology, Investigation. **B. Stelzner:** Writing – review & editing, Supervision. **T. Zirwes:** Writing – review & editing, Supervision, Software. **G. Vignat:** Writing – review & editing, Conceptualization. **F.P. Hagen:** Writing – review & editing, Supervision. **O.T. Stein:** Writing – review & editing, Supervision, Project administration, Funding acquisition, Conceptualization. **M. Ihme:** Writing – review & editing, Conceptualization. **D. Trimis:** Writing – review & editing, Supervision, Project administration, Funding acquisition, Conceptualization.

Declaration of competing interest

The authors declare that they have no known competing financial interests or personal relationships that could have appeared to influence the work reported in this paper.

Acknowledgments

The authors acknowledge the financial support by DFG, Germany (project number: 523876164, within PP2419 HyCAM). The authors also gratefully acknowledge the financial support by the Helmholtz Association of German Research Centers (HGF), Germany, within the research field Energy, program Materials and Technologies for the Energy Transition (MTET), topic Resource and Energy Efficiency, Anthropogenic Carbon Cycle (38.05.01). The authors gratefully acknowledge the Gauss Centre for Supercomputing e.V. (www.gauss-centre.eu) for providing computing time through the John von Neumann Institute for Computing (NIC) on the GCS Supercomputer JUWELS at Jülich Supercomputing Centre (JSC). The authors also gratefully acknowledge the support of the PRIME program of the German Academic Exchange Service (DAAD) with funds from the German Federal Ministry of Education and Research (BMBF), Germany. MI and GV acknowledge financial support through ExxonMobil, USA under agreement LAW-2024-0310.

Data availability

Data will be made available on request.

References

[1] Valera-Medina A, Amer-Hatem F, Azad AK, Dedoussi IC, de Joannon M, Fernandes RX, Glarborg P, Hashemi H, He X, Mashruk S, McGowan J, Mounaim-Rouselle C, Ortiz-Prado A, Ortiz-Valera A, Rossetti I, Shu B, Yehia M, Xiao H, Costa M. Review on ammonia as a potential fuel: From synthesis to economics. Energy Fuels 2021;35(9):6964–7029. http://dx.doi.org/10.1021/acs.energyfuels.0c03685.

[2] Valera-Medina A, Xiao H, Owen-Jones M, David WIF, Bowen PJ. Ammonia for power. Prog Energy Combust Sci 2018;69:63–102. http://dx.doi.org/10.1016/j.pecs.2018.07.001.

[3] Aziz M, Wijayanta AT, Nandiyanto ABD. Ammonia as effective hydrogen storage: A review on production, storage and utilization. Energies 2020;13(12). http://dx.doi.org/10.3390/en13123062.

[4] Kobayashi H, Hayakawa A, Somarathne KKA, Okafor EC. Science and technology of ammonia combustion. Proc Combust Inst 2019;37(1):109–33. http://dx.doi.org/10.1016/j.proci.2018.09.029.

[5] Chai WS, Bao Y, Jin P, Tang G, Zhou L. A review on ammonia, ammonia-hydrogen and ammonia-methane fuels. Renew Sustain Energy Rev 2021;147. http://dx.doi.org/10.1016/j.rser.2021.111254.

[6] Elbaz AM, Wang S, Guiberti TF, Roberts WL. Review on the recent advances on ammonia combustion from the fundamentals to the applications. Fuel Commun 2022;10:100053. http://dx.doi.org/10.1016/j.jfueco.2022.100053.

[7] Lee JH, Kim JH, Park JH, Kwon OC. Studies on properties of laminar premixed hydrogen-added ammonia/air flames for hydrogen production. Int J Hydrog Energy 2010;35(3):1054–64. http://dx.doi.org/10.1016/j.ijhydene.2009.11.071.

[8] Forster P, et al. The earth's energy budget, climate feedbacks, and climate sensitivity, climate change (2021): The physical science basis. contribution of working group I to the sixth assessment report of the intergovernmental panel on climate change. V. Masson-Delmotte et al. Cambridge Univ. Press; 2021, p. 923–1054. http://dx.doi.org/10.1017/9781009157896.009.

[9] Valera-Medina A, Vigueras-Zuniga MO, Shi H, Mashruk S, Alnajideen M, Alnasif A, Davies J, Wang Y, Zhu X, Yang W, Cheng YB. Ammonia combustion in furnaces: A review. Int J Hydrog Energy 2024;49:1597–618. http://dx.doi.org/10.1016/j.ijhydene.2023.10.241.

[10] Mashruk S, Okafor EC, Kovaleva M, Alnasif A, Pugh D, Hayakawa A, Valera-Medina A. Evolution of N_2O production at lean combustion condition in NH_3/H_2/air premixed swirling flames. Combust Flame 2022;244:112299. http://dx.doi.org/10.1016/j.combustflame.2022.112299.

[11] Ravishankara AR, Daniel JS, Portmann RW. Nitrous oxide (N_2O): The dominant ozone-depleting substance emitted in the 21st century. Science 2009;326:123–5. http://dx.doi.org/10.1126/science.1176985.

[12] Okafor EC, Somarathne KDKA, Hayakawa A, Kudo T, Kurata O, Iki N, Kobayashi H. Towards the development of an efficient low-NO_x ammonia combustor for a micro gas turbine. Proc Combust Inst 2019;37(4):4597–606. http://dx.doi.org/10.1016/j.proci.2018.07.083.

[13] Ni S, Zhao D. NO_x emission reduction in ammonia-powered micro-combustors by partially inserting porous medium under fuel-rich condition. Chem Eng J 2022;434. http://dx.doi.org/10.1016/j.cej.2022.134680.

[14] Vignat G, Zirwes T, Boigné É, Ihme M. Experimental demonstration of a two-stage porous media burner for low-emission ammonia combustion. Proc Combust Inst 2024;40(1–4). http://dx.doi.org/10.1016/j.proci.2024.105491.

[15] Yoshida H, Yun J, Echigo R, Tomimura T. Transient characteristics of combined conduction, convection and radiation heat transfer in porous media. Int J Heat Mass Transfer 1990;33(5):847–57. http://dx.doi.org/10.1016/0017-9310(90)90068-6.

[16] Tong T, Sathe S. Heat transfer characteristics of porous radiant burners. J Heat Transf 1991;113(2):423–8.

[17] Trimis D, Durst F. Combustion in a porous medium-advances and applications. Combust Sci Technol 1996;121(1–6):153–68. http://dx.doi.org/10.1080/00102209608935592.

[18] Wood S, Harris AT. Porous burners for lean-burn applications. Prog Energy Combust Sci 2008;34(5):667–84. http://dx.doi.org/10.1016/j.pecs.2008.04.003.

[19] Gharehghani A, Ghasemi K, Siavashi M, Mehranfar S. Applications of porous materials in combustion systems: A comprehensive and state-of-the-art review. Fuel 2021;304. http://dx.doi.org/10.1016/j.fuel.2021.121411.

[20] Takeno T, Sato K, Hase K. A theoretical study on an excess enthalpy flame. Symp Combust 1981;18(1):465–72.

[21] Voss S, Mendes M, Pereira J, Ray S, Pereira J, Trimis D. Investigation on the thermal flame thickness for lean premixed combustion of low calorific H_2/CO mixtures within porous inert media. Proc Combust Inst 2013;34(2):3335–42. http://dx.doi.org/10.1016/j.proci.2012.06.044.

[22] Wang G, Huang L, Tu H, Zhou H, Chen X, Xu J. Stable lean co-combustion of ammonia/methane with air in a porous burner. Appl Therm Eng 2024. http://dx.doi.org/10.1016/j.applthermaleng.2024.123092.

[23] Vignat G, Akoush B, Toro ER, Boigné E, Ihme M. Combustion of lean ammonia-hydrogen fuel blends in a porous media burner. Proc Combust Inst 2023. http://dx.doi.org/10.1016/j.proci.2022.07.054.

[24] Vignat G, Zirwes T, Toro ER, Younes K, Boigné E, Muhunthan P, Simitz L, Trimis D, Ihme M. Experimental and numerical investigation of flame stabilization and pollutant formation in matrix stabilized ammonia-hydrogen combustion. Combust Flame 2023;250:112642. http://dx.doi.org/10.1016/j.combustflame.2023.112642.

[25] Keramiotis C, Stelzner B, Trimis D, Founti M. Porous burners for low emission combustion: An experimental investigation. Energy 2012;45(1):213–9. http://dx.doi.org/10.1016/j.energy.2011.12.006.

[26] Mujeebu MA, Abdullah MZ, Bakar MZA, Mohamad AA, Abdullah MK. Applications of porous media combustion technology – A review. Appl Energy 2009;86(9):1365–75. http://dx.doi.org/10.1016/j.apenergy.2009.01.017.

[27] Nozari H, Tuncer O, Karabeyoglu A. Evaluation of ammonia-hydrogen-air combustion in SiC porous medium based burner. Energy Procedia 2017;142:674–9. http://dx.doi.org/10.1016/j.egypro.2017.12.111.

[28] Kretzler D, Puri R, Stelzner B, Zirwes T, Hagen FP, Stein OT, Trimis D. Experimental and numerical investigation of non-premixed ammonia flames stabilized on a heated slot burner. Proc Combust Inst 2025;41. http://dx.doi.org/10.1016/j.proci.2025.105854.

[29] Zhang F, Zhang G, Wang Z, Wu D, Jangi M, Xu H. Experimental investigation on combustion and emission characteristics of non-premixed ammonia/hydrogen flame. Int J Hydrog Energy 2024;61:25–38. http://dx.doi.org/10.1016/j.ijhydene.2024.02.281.

[30] Chen Y, Zhang B, Su Y, Sui C, Zhang J. Effect and mechanism of combustion enhancement and emission reduction for non-premixed pure ammonia combustion based on fuel preheating. Fuel 2022;308. http://dx.doi.org/10.1016/j.fuel.2021.122017.

[31] Monnery WD, Hawboldt KA, Pollock AE, Svrcek WY. Ammonia pyrolysis and oxidation in the claus furnance. Ind Eng Chem Res 2000;40:144–51.

[32] Benés M, Pozo G, Abían M, Millera A, Bilbao R, Alzueta MU. Experimental study of the pyrolysis of NH_3 under flow reactor conditions. Energ Fuel 2021;35(9):7193–200. http://dx.doi.org/10.1021/acs.energyfuels.0c03387, URL https://www.ncbi.nlm.nih.gov/pubmed/35673549.

[33] Sobhani S, Mohaddes D, Boigne E, Muhunthan P, Ihme M. Modulation of heat transfer for extended flame stabilization in porous media burners via topology gradation. Proc Combust Inst 2018;37(4):5697–704. http://dx.doi.org/10.1016/j.proci.2018.05.155.

[34] Vásárhelyi L, Kónya Z, Kukovecz A, Vajtai R. Microcomputed tomography–based characterization of advanced materials: a review. Mater Today Adv 2020;8:100084. http://dx.doi.org/10.1016/j.mtadv.2020.100084.

[35] Ferguson JC, Semeraro F, Thornton JM, Panerai F, Borner A, Mansour NN. Update 3.0 to "PuMA: The porous microstructure analysis software". SoftwareX 2021;15:100775.

[36] Otsu N. A threshold selection method from gray-level histograms. IEEE Trans Sys Man Cyber 1979;9(1):62–6.

[37] Puri R, Kretzler D, Bock-Seefeld B, Stelzner B, Brachhold N, Hubálková J, Trimis D, Aneziris C, Stein OT, Zirwes T. Influence of dispersion length on volume-averaged simulations of ammonia/air combustion in porous media burners. Proc Combust Inst 2025;41:105856. http://dx.doi.org/10.1016/j.proci.2025.105856.

[38] Jacimovic B, Genic S, Lelea D. Calculation of the heat transfer coefficient for laminar flow in pipes in practical engineering applications. Heat Transf Eng 2018;39(20):1790–6. http://dx.doi.org/10.1080/01457632.2017.1388949.

[39] Zirwes T, Vignat G, Toro ER, Boigné E, Younes K, Trimis D, Ihme M. Improving volume-averaged simulations of matrix-stabilized combustion through direct X-ray μ CT characterization: Application to NH3/H2-air combustion. Combust Flame 2023;257:113020.

[40] Navaneethakrishnan P, Krishnakumar K, Anish KJ. Effect of perforation shape and porosity on effective thermal conductivity of matrix heat exchanger plates. Appl Therm Eng 2016;106:432–7. http://dx.doi.org/10.1016/j.applthermaleng.2016.06.024.

[41] Wieland C, Weis C, Habisreuther P, Trimis D. 3D direct pore level simulations of radiant porous burners. Combust Flame 2022;245:112370.

[42] Bidi M, Nobari M, Avval MS. A numerical evaluation of combustion in porous media by EGM (entropy generation minimization). Energy 2010;35(8):3483–500.

[43] Shuai L, Lars D, Shia-Hui P. A pressure-loss model for flow-through round-hole perforated plates of moderate porosity and thickness in laminar and turbulent flow regimes. Int J Heat Mass Transfer 2024;226:125490. http://dx.doi.org/10.1016/j.ijheatmasstransfer.2024.125490.

[44] Baukal CE, Eleazer PB. Quantifying NO_x for industrial combustion processes. J Air Waste Manage Assoc 1998;48(1):52–8. http://dx.doi.org/10.1080/10473289.1998.10463664.

[45] Brenner G, Pickenäcker K, Pickenäcker O, Trimis D, Wawrzinek K, Weber T. Numerical and experimental investigation of matrix-stabilized methane/air combustion in porous inert media. Combust Flame 2000;123(1):201–13.

[46] Stagni A, Cavallotti C, Arunthanayothin S, Song Y, Herbinet O, Battin-Leclerc F, Faravelli T. An experimental, theoretical and kinetic-modeling study of the gas-phase oxidation of ammonia. React Chem Eng 2020;5:696–711.

[47] Zhu Y, Curran HJ, Girhe S, Murakami Y, Pitsch H, Senecal K, Yang L, Zhou C-W. The combustion chemistry of ammonia and ammonia/hydrogen mixtures: A comprehensive chemical kinetic modeling study. Combust Flame 2024;260:113239. http://dx.doi.org/10.1016/j.combustflame.2023.113239.

[48] Zhang X, Moosakutty SP, Rajan PR, Younes M, Sarathy SM. Combustion chemistry of ammonia/hydrogen mixtures: Jet-stirred reactor measurements and comprehensive kinetic modeling. Combust Flame 2021;234:111653.
[49] Konnov AA. An exploratory modelling study of chemiluminescence in ammonia-fuelled flames. Part 1. Combust Flame 2023;253.
[50] Konnov AA. An exploratory modelling study of chemiluminescence in ammonia-fuelled flames. Part 2. Combust Flame 2023;253.
[51] Shrestha KP, Lhuillier C, Barbosa AA, Brequigny P, Contino F, Mounaïm-Rousselle C, Seidel L, Mauss F. An experimental and modeling study of ammonia with enriched oxygen content and ammonia/hydrogen laminar flame speed at elevated pressure and temperature. Proc Combust Inst 2021;38(2):2163–74. http://dx.doi.org/10.1016/j.proci.2020.06.197.
[52] Mei B, Zhang J, Shi X, Xi Z, Li Y. Enhancement of ammonia combustion with partial fuel cracking strategy: Laminar flame propagation and kinetic modeling investigation of $NH_3/H_2/N_2$/air mixtures up to 10 atm. Combust Flame 2021;231. http://dx.doi.org/10.1016/j.combustflame.2021.111472.